



## Mouse long-chain acyl-CoA synthetase 1 is active as a monomer

Holly Dykstra, Chelsea Fisk, Cassi LaRose, Althea Waldhart, Xing Meng, Gongpu Zhao, Ning Wu\*

Van Andel Institute, Grand Rapids, MI, 49503, USA

### ARTICLE INFO

#### Keywords:

Acyl-CoA synthetase  
Fatty acid metabolism  
Structure-function  
Electron microscopy  
Nanodisc  
Enzyme kinetics

### ABSTRACT

Fatty acids are essential cellular building blocks and a major energy source. Regardless of their metabolic fate, fatty acids first need to be activated by forming a thioester with a coenzyme A group. This reaction is carried out by acyl-CoA synthetases (ACSSs), of which ACSL1 (long-chain acyl-CoA synthetase 1) is an important member. Two bacterial homologues of ACSL1 crystal structures have been solved previously. One is a soluble dimeric protein, and the other is a monomeric peripheral membrane protein. The mammalian ACSL1 is a membrane protein with an N-terminal transmembrane helix. To characterize the mammalian ACSL1, we purified the full-length mouse ACSL1 and reconstituted it into lipid nanodiscs. Using enzymatic assays, mutational analysis, and cryo-electron microscopy, we show that mouse ACSL1 is active as a monomer.

### 1. Introduction

Fatty acids (FAs)<sup>1</sup> are essential to cellular function. They need to be activated by conjugating to coenzyme A (CoA) in order to be used for  $\beta$ -oxidation, incorporation into phospholipids, or neutral lipid synthesis. Acyl-CoA synthetases (ACSSs) are classified into families according to the chain length of their substrates: those families are named short-chain ACS (ACSS), medium-chain ACS (ACSM), long-chain ACS (ACSL), very long-chain ACS (ACSVL), Bubblegum ACS (ACSBG), and ACS family (ACSF) [1]. The ACSL family is particularly important because those enzymes esterify free FAs of 12–20 carbons, which are prevalent in the human diet. There are five ACSL isoforms, and they differ in their tissue distribution, subcellular localization, and substrate preference [2]. ACSL1 is expressed in many tissues, and especially highly in liver and adipose tissue. It is found in the plasma membrane, outer membrane of mitochondria, and the ER, depending on the cell type [3]. The first of the two classic roles of ACSL1 is facilitating FA transport across the plasma membrane where CoA attachment prevents free FAs from diffusing back out of the cell [4]. The second role is channeling FAs toward  $\beta$ -oxidation [5]. On the mitochondrial outer membrane, ACSL1 delivers acyl-CoA to CPT1 proteins for conversion into acyl-carnitine, which then enters the mitochondria for FA oxidation [3,6]. ACSL1 has been reported to

interact with various protein networks to orchestrate FA metabolism [3].

The current structural understanding of mammalian ACSL comes largely from bacterial crystal structures. The crystal structures of a *Thermus thermophilus* ACSL homologue, ttLC-FACS [7], and a *Mycobacterium tuberculosis* ACSVL homologue, FadD13 [8], have been reported. ttLC-FACS has substrate length ranging from 12 to 18 carbons. It is a soluble enzyme that works as a dimer with two independent active sites. FadD13 is a membrane-bound peripheral enzyme that functions as a monomer with substrate carbon length up to C26. Both share a two-domain structure, having a large N-terminal domain and a small C-terminal domain. During the reaction, the C-terminal domain moves towards the N-terminal domain to complete the active site [9]. The general catalytic mechanism for these enzymes is thought to involve two steps. First, the free FA condenses with ATP to form an acyl-AMP intermediate with a release of pyrophosphate. Second, the intermediate binds CoA, which replaces the AMP. In the FadD13 structure, membrane attachment could allow the reaction to occur without completely extracting the FA from the membrane. Unlike either of the bacterial proteins, mammalian ACSL1 is a membrane protein with a single N-terminal transmembrane helix predicted by sequence analysis [3]. For the mouse protein, it is amino acids <sup>25</sup>LPTNTLMGFGA-FAALTFWYA<sup>45</sup>, which is 100% conserved between human, mouse, and

\* Corresponding author.

E-mail address: [Ning.wu@vai.org](mailto:Ning.wu@vai.org) (N. Wu).

<sup>1</sup> The abbreviations used are: FA, fatty acid; CoA, coenzyme A; ACS, acyl-CoA synthetase; ACSL1, long-chain ACS 1; ACSS, short-chain ACS; ACSM, medium-chain ACS; ACSVL, very long-chain ACS; ACSBG, Bubblegum ACS; ACSF, ACS family; ER, endoplasmic reticulum; CPT, carnitine palmitoyl transferase; ttLC-FACS, long-chain fatty ACS from *T. thermophilus* HB8; FadD13, bacterial fatty ACS; MSP, membrane scaffold protein; SMA, styrene-maleic acid copolymer; cryo-EM, cryo-electron microscopy; EM, electron microscopy; 2D, two-dimensional; AppNp, adenosine 5'-( $\beta$ ,  $\gamma$ -imidio) triphosphate; HPLC, high performance liquid chromatography.

<https://doi.org/10.1016/j.abbi.2021.108773>

Received 31 October 2020; Received in revised form 15 January 2021; Accepted 16 January 2021

Available online 21 January 2021

0003-9861/© 2021 Elsevier Inc. All rights reserved.

rat ACSL1. It is unclear whether this N-terminal transmembrane helix of ACSL1 is important for catalysis. It is also unclear whether the mammalian ACSL1 is a monomer or a dimer.

One of the difficulties of working with membrane proteins is the need for detergent to keep the proteins in solution. Detergents can adversely affect protein stability and function. Recently, methods have been

developed to enclose membrane proteins and the lipids together, using either lipid-binding proteins or polymers to generate soluble protein-lipid particles called nanodiscs [10–12]. These methods use engineered derivatives of apolipoprotein A1 scaffold proteins (called membrane scaffold protein, MSP), saposin A, and styrene-maleic acid copolymer (SMA). These have proven to be useful in enzyme activity assays without detergent and

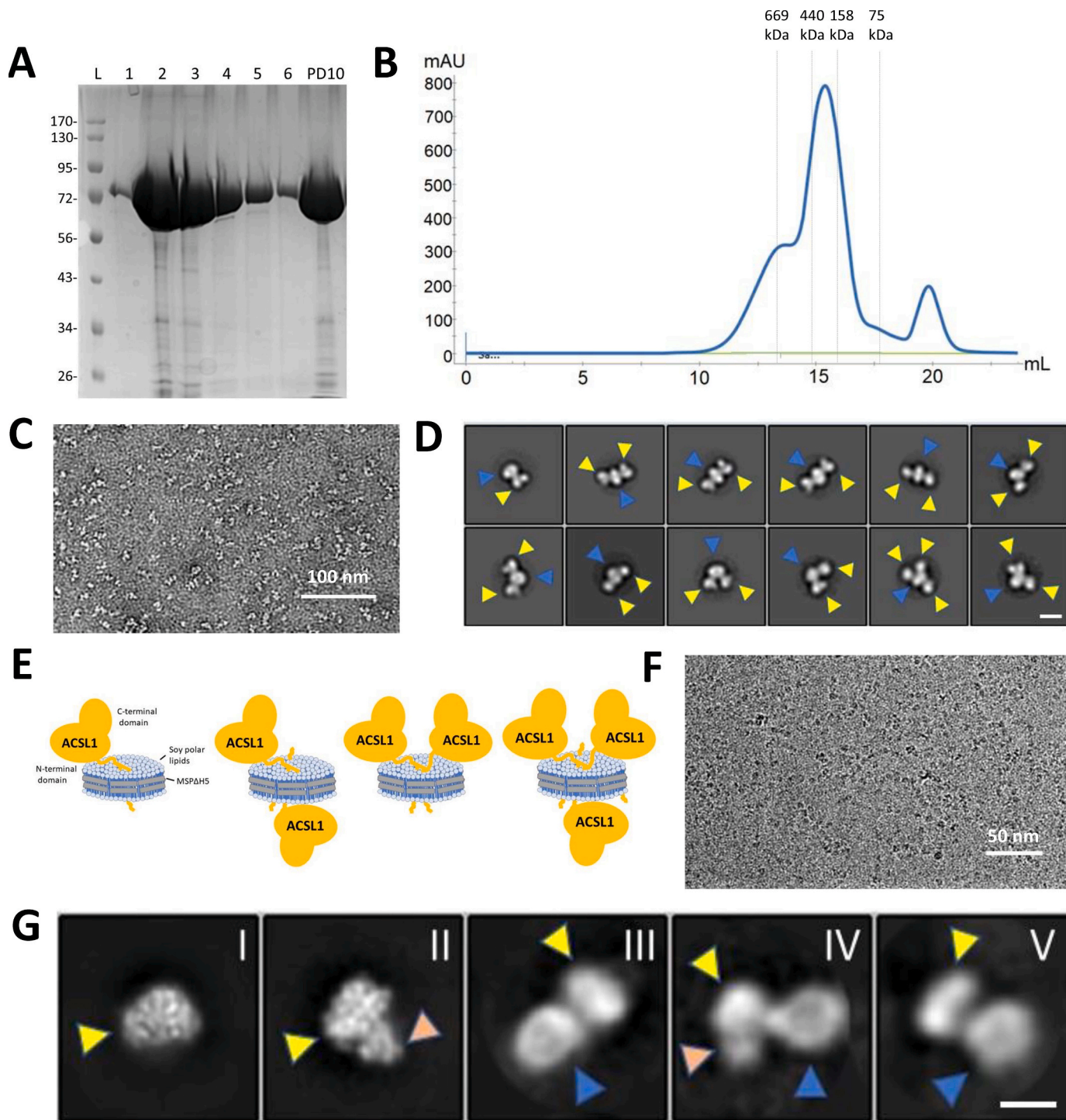


**Fig. 1.** Full-length ACSL1 is a monomer by EM. (A). ACSL1 elution fractions 1 to 6 from Ni-NTA. The last lane is the PD10 buffer-exchanged protein after the Ni-NTA column. (B). Superose 6 FPLC elution profile of ACSL1/soy polar lipids/MSPΔH5 nanodiscs. Standard molecular weight markers are indicated by dashed lines. (C). A representative negative-stain EM micrograph of ACSL1 nanodiscs. (D). 2D class averages from negative-stain images, showing multiple ways of ACSL1 insertion into the nanodisc. Yellow arrowheads point to ACSL1 and blue arrowheads to the nanodisc. Scale bar represents 10 nm. (E). A schematic model of the various methods of ACSL1 insertion into nanodisc. (F). A representative cryo-EM micrograph at 30,000× magnification. (G). Representative cryo-EM 2D class averages of ACSL1 alone (I and II) or in complex with the nanodisc (III–V). ACSL1 in complex with nanodisc had poorer resolution. Yellow arrowheads point to ACSL1 and blue arrowheads to the nanodisc. Orange arrowheads point to the C-terminal domain in the open position. Scale bar represents 5 nm.

in high-resolution structural determinations by cryo-electron microscopy (cryo-EM). Among the different types of protein–lipid particles, MSP is relatively easy to use, and MSPs of different lengths have been developed to generate nanodiscs of different sizes.

In this study, we successfully purified the full-length mouse ACSL1 and reconstituted it into nanodiscs using MSP $\Delta$ H5, eliminating the need to use detergents during enzyme assays. Using cryo-EM single-particle analysis and an N-terminal-truncated version of ACSL1, we show that mouse ACSL1 is active as a monomer.

## 2. Results

### 2.1. ACSL1 incorporates into lipid nanodiscs as a monomer

ACSL1 is predicted to have a single transmembrane segment at the N-terminus. Since the lipid environment may influence the function of the enzyme, we decided to express the full-length protein in insect cells to ensure proper incorporation of the protein into the membrane. Mouse ACSL1 with a C-terminal His10 tag was cloned into the pFastBac system and expressed in High Five cells. The protein expressed and purified well using Ni-NTA affinity resin (Fig. 1A). The eluted protein was quickly buffer-exchanged to eliminate the high concentration of imidazole using a PD10 column and then was mixed with soy polar lipids that had already been sonicated into small unilamellar liposomes. Then MSP $\Delta$ H5 was added to encircle the protein within the lipid/detergent mixture; the detergent was eliminated using biobeads. A typical size distribution of ACSL1/MSP $\Delta$ H5 nanodiscs on an analytical Superose 6 column is shown in Fig. 1B. The center fraction of the peak at about 15 mL was used for single-particle analysis by electron microscopy (EM).

First, we used negative-stain EM to analyze the oligomeric state of ACSL1. The micrographs showed good particle distribution and density and allowed visualization of the complex (Fig. 1C). The resulting reference-free, two-dimensional (2D) classes showed that ACSL1 has different ways to insert into the nanodisc (Fig. 1D and E). If the mouse ACSL1 works as a dimer, then the MSP $\Delta$ H5 would most likely enclose a dimer together in one nanodisc. However, our negative-stain data indicated that while multiple ACSL1 monomers were often incorporated into a single nanodisc, they did not appear to be interacting. Indeed, some 2D classes showed ACSL1 monomers inserting on opposite sides of the nanodisc, while other classes showed two monomers on the same side but with no apparent interaction. This observation led us to speculate that ACSL1 is a monomer.

To investigate ACSL1 structure at higher resolution, we examined our sample via cryo-EM. ACSL1 is about 75 kDa, which is small for high-resolution, single-particle analysis by cryo-EM. The bacterial enzyme structures suggest that ACSL1 has two domains with the enzyme active site formed at their interface [7,8]. The smaller C-terminal domain can move away from the larger N-terminal domain to allow substrate binding and product release. This variable conformational positioning between the two domains increases the difficulty of particle alignment in 2D classification. Therefore, we tested various substrates and products homologues in search of the most stable complex for cryo-EM study.

We found that the combination best for enzyme stability and cryo-EM was AppNp (a nonhydrolyzable ATP analogue) and C18:1 (oleic acid). Cryo-EM images showed that the particles were monodisperse (Fig. 1F). Particles were autopicked from collected micrographs and then were subjected to iterative, reference-free, 2D classifications. The resulting classes showed ACSL1 complexed with the disc-like density of the nanodisc in some classes, while in others, ACSL1 appears to have broken away from the nanodiscs (Fig. 1G). Despite changing the grid-freezing parameters, we continued to see the same results. The resolution of 2D classes of ACSL1 alone was superior to the resolution of 2D classes of ACSL1 in complex with nanodiscs. There are many reasons for this, including 1) the nanodisc orientation relative to ACSL1 is not fixed, and 2) the ACSL1 soluble domain is relatively small compared with the nanodisc. However, it is clear from the 2D classes that ACSL1 exists as a monomer.

### 2.2. Full-length ACSL1 is active in nanodiscs

Because detergents used in membrane protein isolation and stabilization can directly affect ACSL1 activity, we hypothesized that purification and reconstitution into nanodiscs could provide a more native environment for assessing enzymatic kinetics. Using the full-length ACSL1 in nanodiscs, we performed ACSL1 activity assays using oleate (C18:1) as a substrate at concentrations ranging from 10  $\mu$ M to 500  $\mu$ M and with saturating amounts of CoA and ATP. The product (AMP) was monitored by HPLC (Fig. 2A and B). No detergent was present during the assay. We found that the full-length protein was active and had a relative  $K_m$  of  $58 \pm 4$   $\mu$ M for C18:1, which is on the lower end of the normal plasma oleic acid concentration of 30  $\mu$ M to 3.2 mM [13].

Due to the sequence homology between the *T. thermophilus* tLc-FACS and the mammalian ACSL [7], we hypothesized that the conserved T277 and E463 in the mouse ACSL1 are important active site residues, and that mutation of these two residues into alanine should render the enzyme inactive. We therefore made a double alanine (AA) mutant (T277A/E463A) and inserted it into the MSP $\Delta$ H5 nanodiscs. The mutant protein behaved similarly to the wild type during purification (Fig. 2C), and just as expected, it was enzymatically inactive (Fig. 2D). This finding lends strength to our purification methods.

### 2.3. ACSL1 $\Delta$ 58 is catalytically active as a soluble enzyme

Cryo-EM data (Fig. 1G) showed that during grid freezing, some ACSL1 protein broke away from the nanodiscs. In addition, sequence alignment of FadD13 and mouse ACSL1 showed none of the arginine residues important for FadD13 association with the membrane are conserved in mouse ACSL1 (Supplementary Fig. 1). We wondered whether we could get higher-resolution structures by just analyzing the soluble catalytic portion of mouse ACSL1. We deleted amino acids 1–57 to eliminate the transmembrane region and some of the flexible linker region. The  $\Delta$ 58 truncated protein was expressed in High Five cells to be consistent. It was soluble, so we purified it from the cell lysate supernatant fraction instead of the membrane fraction. No detergent was used during the purification. Compared with the full-length protein in nanodisc,  $\Delta$ 58 was less stable and tended to precipitate out upon storage at 4 °C. For the cryo-EM work, we added AppNp and C18:1 to stabilize the protein, and for the enzymatic work we used freshly prepared protein to minimize protein inactivation. As shown in Fig. 3A,  $\Delta$ 58 complexed with AppNp and C18:1 ran as a single peak on Superdex 200. We used SDS-PAGE and BSA standards to estimate the ACSL1 protein concentration (Fig. 3B). Using the same amount of protein as for full-length WT ACSL1, we found the  $\Delta$ 58 still had activity, although the  $K_m$  was larger than the full-length protein (Fig. 3C). Nevertheless, the results support the idea that mouse ACSL1 is active as a monomer.

### 2.4. The Cryo-EM structure of $\Delta$ 58 shows folding similar to that of bacterial homologues

Next, we attempted to determine the structure of  $\Delta$ 58 ACSL1 via cryo-EM to confirm it is a monomer. We assessed sample density and distribution (Fig. 4A) and collected a modest-sized data set on Krios (about 3400 micrographs). After picking particles and eliminating poor-quality particles through iterative 2D classifications, the two-domain structure can be seen in some 2D classes (Fig. 4B).

Using a total of 83,000 particles, the 3D reconstruction of  $\Delta$ 58 ACSL1 revealed two possible conformations, open (26% of particles) and closed (52% of particles) (Fig. 4C). The remaining particles fell into classes with poorly defined features (Supplementary Fig. 2). Further refinement of each conformation was low-pass-filtered to a resolution of 10 Å with an adjusted threshold of 0.0013 for the open conformation and with an adjusted threshold of 0.0027 for the closed conformation. Comparing the size of these two dominant classes with the crystal structure of FadD13, they matched quite closely (Fig. 4C and D). This clearly supports that  $\Delta$ 58 ACSL1 is a monomer.

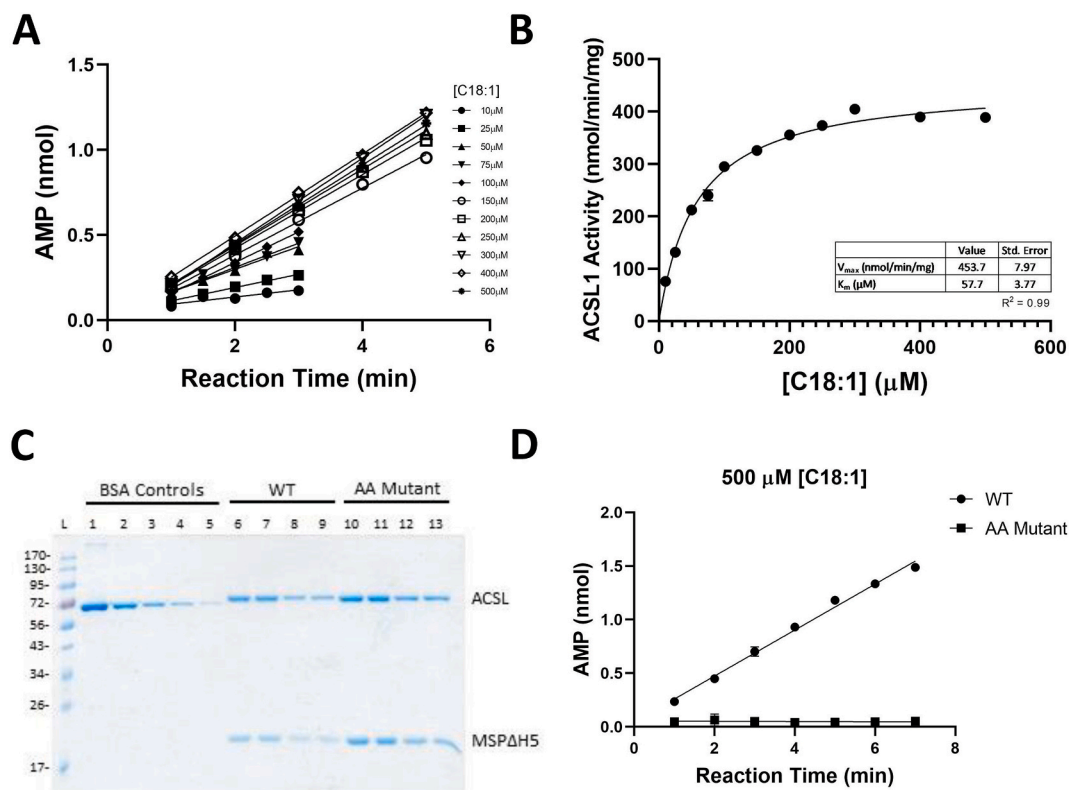


**Fig. 2.** Enzyme kinetics of ACSL1 nanodisc with oleic acid. (A). Initial velocity with various concentrations of oleic acid (C18:1). (B). Michaelis–Menten kinetic enzyme activity curves from purified, full-length ACSL1 assayed with oleic acid. (C). Protein gel of ACSL1 full-length wild type (WT) and AA (double alanine) mutant used to standardize the amounts of protein used for activity comparison. L = ladder; 1–5 = BSA standards (1 = 250  $\mu$ g/mL, 2 = 125  $\mu$ g/mL, 3 = 50  $\mu$ g/mL, 4 = 25  $\mu$ g/mL, 5 = 5  $\mu$ g/mL); 6–7 = WT samples in duplicate; 8–9 = WT sample 1:2 dilution in duplicate; 10–11 = AA mutant in duplicate; 12–13 = AA mutant 1:2 dilution in duplicate. (D). Initial velocities comparison of WT and AA mutant at 500  $\mu$ M C18:1. Results are mean  $\pm$  SD. When no error bars appear, the SD values were smaller than the symbols.

### 3. Discussion

We report the expression, purification, and lipid nanodisc insertion of the mouse ACSL1 protein along with a low-resolution structure of the mouse ACSL1 catalytic domain by cryo-EM. The major conclusion is mouse ACSL1 has the same two-domain architecture as ttLC-FACS and FadD13. The AA mutant data and the sequence homology [7] supports that mouse ACSL1 works as a monomer and follows the same catalytic steps as that reported for ttLC-FACS.

The difficulties of studying the kinetics of lipid-modifying enzymes include the extraction and purification of membrane-bound proteins from their hydrophobic environment while keeping them stable and active. The detergents used for protein purification can introduce artifacts because the enzyme may need the native lipid to function properly. We used fos-choline 12 to extract ACSL1, quickly replaced the detergent with soy polar lipids, and then successfully enclosed ACSL1 and lipids in MSP $\Delta$ H5 nanodiscs. This stabilized ACSL1 and we could carry out kinetic assays without any detergent. Compared to the published values [14], our  $K_m$  of the full-length ACSL1 was larger ( $58 \pm 4$   $\mu$ M vs.  $6.7 \pm 1.4$   $\mu$ M) and the  $V_{max}$  was smaller ( $454 \pm 8$  nmol/min/mg vs.  $2089 \pm 108$   $\mu$ mol/min/mg), likely due to these modifications. In addition, cyclodextrin was used in the reaction to keep the oleic acid in solution because no detergent was present. This may affect the accessibility and kinetics of the ACSL1 and oleic acid interaction. As to the real specific activity *in vivo*, there are more parameters to be considered, such as the local availability/concentration of FAs and whether the substrate needs to be delivered to the enzyme via a FA-binding protein.

From our negative-stain EM studies, one can see that multiple ACSL1 proteins can be enclosed within one MSP $\Delta$ H5 nanodisc, sometimes on the same side of the nanodisc and sometimes on opposite sides. It is clear

that individual ACSL1 proteins do not interact with each other. The  $\Delta$ 58 truncation later confirmed that ACSL1 is active as a monomer. However, it is important to point out that  $\Delta$ 58 (especially the apo protein) was much less stable than the full-length protein in nanodiscs during storage at 4  $^{\circ}$ C and was less active than the full-length protein. Protein stability may contribute to the lower  $V_{max}$  of  $\Delta$ 58. The higher  $K_m$  value for  $\Delta$ 58 may indicate that the membrane surface may be important for maximum catalytic efficiency of ACSL. There are about 40 amino acid linkers predicted between the transmembrane helix and the rest of the folded structure. From the EM images, we did not detect any significant association of the soluble folded domains with the nanodisc lipid surface. In fact, the ACSL1 and the nanodisc seem to be able to rotate freely relative to each other. Therefore, we do not know how the transmembrane helix or the close proximity to the lipid surface contribute to catalysis.

From our cryo-EM studies on the full-length ACSL1 in nanodiscs, we found the conditions used to freeze EM grids were harsh enough to cause some protein to come out of its lipid environment. This was quite surprising to us. We do not know if this property is generally true for single transmembrane proteins or is specific to ACSL1. However, it has been reported that the air-water interface is detrimental to low affinity protein complexes and can even cause protein denaturation [15,16]. This freezing effect may possibly affect the ligand occupancy in our  $\Delta$ 58 structure. We saturated the protein solution with ligands before freezing the grids, so we should only see one closed conformation. However, the final classification showed two major conformations, not just one. The open conformation implies that the ligands must have dissociated from the protein.

One important function of ACSL1 is to provide acyl-CoA to CPT1 for transport into the mitochondria for oxidation. Two known ways that FA oxidation can be regulated via CPT1A is its expression increase induced by high fat content in diet [17] and by the inhibition of CPT1 activity by

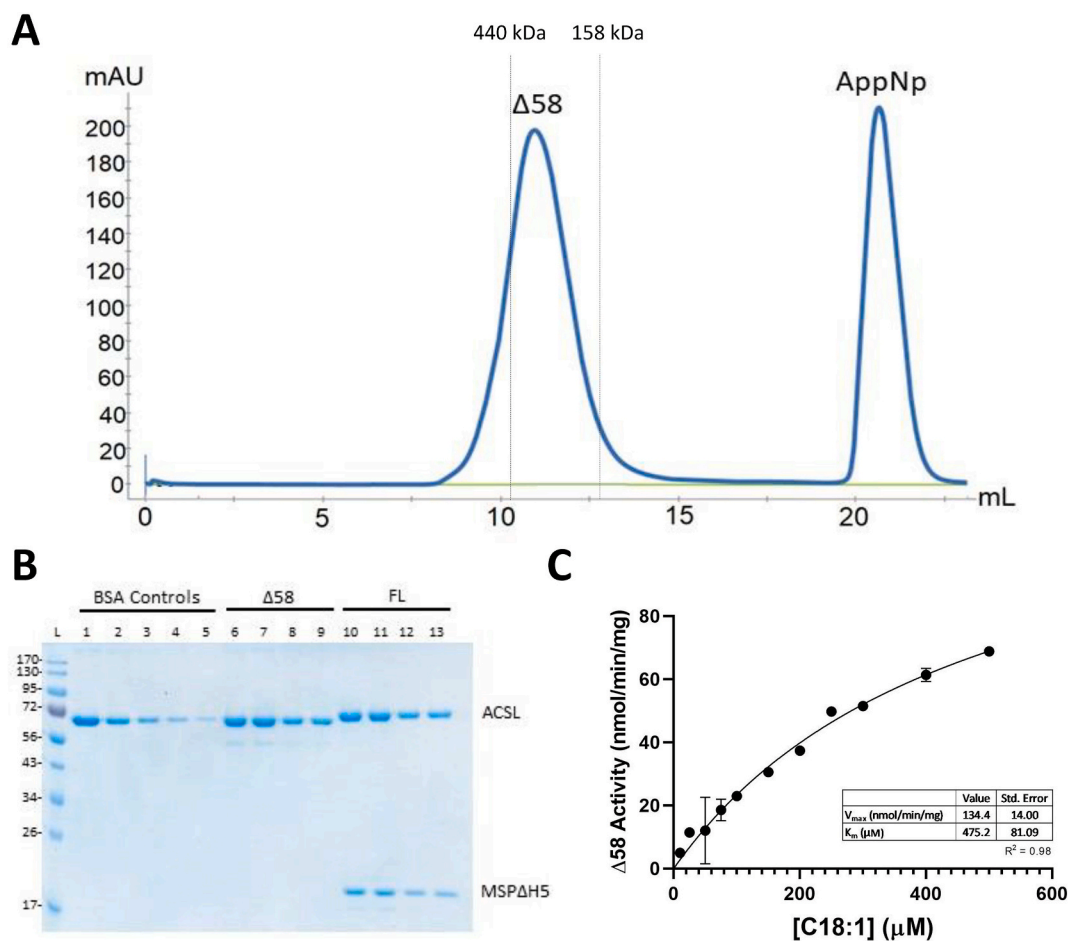


**Fig. 3.** Truncation mutant  $\Delta 58$  purification and activity. (A). Superdex 200 FPLC elution of  $\Delta 58$  ACSL1 at about 11 mL. The second peak is AppNp added to stabilize the protein. Standard molecular weight markers are indicated by dashed lines. (B). Protein gel of  $\Delta 58$  and full-length (FL) ACSL1 showing the relative amount of protein used for activity assay. L = ladder; 1–5 = BSA standards (1 = 250  $\mu\text{g}/\text{mL}$ , 2 = 125  $\mu\text{g}/\text{mL}$ , 3 = 50  $\mu\text{g}/\text{mL}$ , 4 = 25  $\mu\text{g}/\text{mL}$ , 5 = 5  $\mu\text{g}/\text{mL}$ ); 6–7 =  $\Delta 58$  in duplicate; 8–9 =  $\Delta 58$  1:2 dilution in duplicate; 10–11 = FL in duplicate; 12–13 = FL 1:2 dilution in duplicate. (C). Michaelis–Menten kinetic enzyme activity curves from purified  $\Delta 58$  ACSL1 assayed with oleate (C18:1). Results are mean  $\pm$  SD. When no error bars appear, the SD values were smaller than the symbols.

malonyl-CoA [18], product of FA synthesis. In addition, CPT1A has been reported to be an oligomer [19] that shifts between hexameric and trimeric states [20,21]. It is conceivable that ACSL1 interaction with CPT1A is also regulated by metabolic demands. Knowing that ACSL1 is a monomer can help clarify the structure-function of ACSL1 and its relationship with associated proteins.

## 4. Methods and materials

### 4.1. Cloning

Mouse ACSL1 was cloned into a homemade pFastBac1-His10 vector at BamHI and NotI sites, with His10 tag at the C-terminus. Baculovirus was generated from SF9 cells according to the Bac-to-Bac manufacturer's instructions (Invitrogen). High Five cells were infected with the baculovirus for protein production.

### 4.2. Protein purification

Soy polar lipids (Avanti 541602) in chloroform were dried with nitrogen gas and rehydrated with buffer (30 mM Tris pH 7.5, 50 mM NaCl, 0.1 mM  $\text{MgSO}_4$ ) and probe-sonicated to prepare unilamellar, uniform liposomes. Soy PC (95%) (Avanti 441601) was similarly rehydrated in resuspension buffer (25 mM Tris 7.5, 150 mM NaCl, 10 mM  $\text{MgSO}_4$ , 5% glycerol, 0.2% fos-choline 12) and probe-sonicated.

The frozen cells were thawed and mechanically homogenized with a Teflon tissue homogenizer. Cell membranes were collected by centrifugation and solubilized with resuspension buffer (25 mM Tris 7.5, 150 mM NaCl, 10 mM  $\text{MgSO}_4$ , 5% glycerol, 0.2% fos-choline 12). For purification of the recombinant protein, the supernatant was batch bound with Ni-NTA beads (Qiagen) for 1 h and was packed into an empty PD10 column and washed with 25 mM Tris 7.5, 150 mM NaCl, 30 mM imidazole, 10 mM  $\text{MgSO}_4$ , 5% glycerol, 0.00125% soy PC (95%), and 0.05% fos-choline 12. Protein was eluted with 300 mM imidazole in the wash buffer. The most concentrated fractions were buffer-exchanged into 30 mM Tris 7.5, 50 mM NaCl, 0.5 mM  $\text{MgSO}_4$ , 0.00125% soy PC (95%), and 0.05% fos-choline 12 using a PD10 column. Soy polar lipids were added to the buffer-exchanged protein. For stabilization, 0.5 mM AppNp and 0.15 mM oleic acid were added, chosen specifically for their compatibility with future structural analysis. Following a 2 h incubation period, MSP $\Delta$ H5 was added for 1 h. BioBeads were added overnight to adsorb fos-choline 12. The resulting nanodiscs were concentrated using a 30-kDa cut-off concentrator and loaded onto an analytical Superose 6 SEC column, equilibrated with 30 mM Tris, pH 7.5, 50 mM NaCl, and 0.25 mM TCEP. The correct fractions were collected and stored on ice for further analysis.

### 4.3. Enzyme activity assay

Enzyme activity was measured by AMP formation as analyzed on an HPLC (Dionex Ultimate 3000 UHPLC+) at 259 nm. The reaction

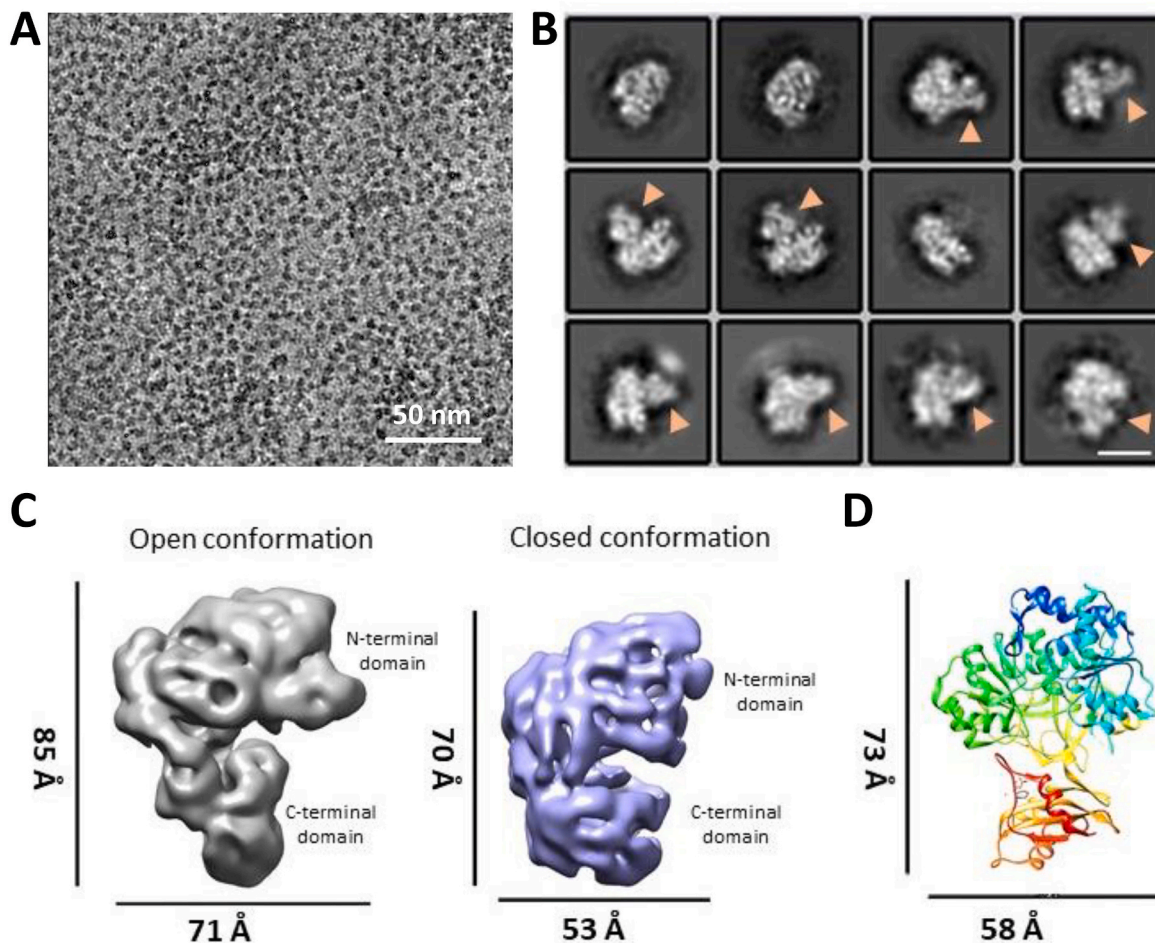


**Fig. 4.** Single-particle cryo-EM analysis of  $\Delta 58$  complexed with AppNp and C18:1. (A). A representative cryo-EM micrograph at 215,000 $\times$  magnification. (B). Representative 2D class averages showing secondary structure elements of  $\Delta 58$  ACSL1. Orange arrowheads point to the C-terminal domain in the open position. Scale bar represents 5 nm. (C). The  $\Delta 58$  ACSL1 single-particle reconstruction in the open (left) and closed (right) conformation. 3D reconstructions were low-pass-filtered to 10  $\text{\AA}$  with a raised threshold of 0.0013 (open) and 0.0027 (closed). (D). Rainbow coloring from blue (N-terminal) to red (C-terminal) of the previously published *Mycobacterium tuberculosis* FadD13 crystal structure (PDB ID: 3R44) with comparable dimensions and shape to the  $\Delta 58$  ACSL1 3D reconstruction.

was carried out in 30 mM Tris 7.5, 50 mM NaCl, 0.5 mM  $\text{MgSO}_4$ , 2.5 mg/mL cyclodextrin, with 200  $\mu\text{M}$  CoA, 1 mM ATP, and various concentrations of oleic acid. The reaction was allowed to proceed for between 1 and 7 min. Each time point was terminated with chloroform. Chloroform extraction was performed a second time to remove all protein and lipids. The resulting aqueous sample was mixed with an equal amount of 5% perchloric acid for AMP stability then run isocratically with a mobile phase (100 mM sodium acetate, 75 mM monosodium phosphate, pH 4.6) on a C18 column (Thermo fisher BDS Hypersil). Michaelis–Menten kinetic enzyme activity curves were drawn, and  $V_{\text{max}}$  and  $K_{\text{m}}$  values were calculated using GraphPad Prism 8.0.

#### 4.4. Negative-staining electron microscopy

To determine sample quality and incorporation into the nanodisc, negative-stain grids were prepared and imaged. The protein sample was applied to a freshly plasma-cleaned, carbon-coated, copper grid (300-mesh, EMS) for 1 min. Grids were then blotted and stained with two 20  $\mu\text{L}$  droplets of 2% uranyl formate. Images were collected at a nominal 30,000 $\times$  magnification on a Thermo Fisher Scientific Tecnai Spirit G2 BioTWIN microscope at 120 kV with a Gatan Orius 830 CCD camera. Image analysis, particle picking, and 2D class averaging were performed using RELION 3.0 [22].

#### 4.5. Cryo-EM sample preparation and data acquisition

Quantifoil R1.2/1.3 300-mesh Au grids (SPI) were used with all samples. In our case, negative glow discharging of the grids led to a strongly preferred orientation of our ACSL1 complexes. We also suspected denaturation of our complex at the air–water interface. Orientational bias makes three-dimensional analysis very challenging so we experimented with alternate methods of positive glow-charging. We had the best results when grids were glow-discharged in the presence of amylamine for 20 s which yielded positively charged grids and improved particle orientation. The protein sample (3  $\mu\text{L}$ ) was applied to the grids, blotted for 4 s, and then plunge-frozen in liquid ethane using a Thermo Fisher Scientific Vitrobot Mark IV at 100% RH and 4  $^{\circ}\text{C}$ .

For ACSL1 in lipid nanodiscs: Cryo-EM data was collected using the Thermo Fisher Scientific Talos Arctica electron microscope operating at 200 kV. Images were acquired with a K2 Summit direct detection camera (Gatan) operating in counting mode at a nominal 36,000 $\times$  magnification, corresponding to a calibrated physical pixel size of 1.156  $\text{\AA}$  with a defocus range between  $-1.5$  and  $-2.1$   $\mu\text{m}$ , using SerialEM, an automated acquisition program [23]. Each micrograph was exposed for 6 s with 10  $\text{e}^-/\text{\AA}^2/\text{s}$  dose rate (total accumulated dose, 60  $\text{e}^-/\text{\AA}^2$ ), and about 30 frames were captured per movie stack.

For  $\Delta 58$  ACSL1: Cryo-EM data were collected using the Thermo Fisher Scientific Titan Krios electron microscope operating at 300 kV,

aligned for parallel illumination. Images were acquired with a K2 Summit direct detection camera (Gatan) and a phase plate (FEI) operating in super-resolution counting mode at a nominal 215,000 $\times$  magnification, with a super-resolution pixel size of 0.629 Å. Over a period of 3 d, 3398 images with defocus values ranging from  $-0.4$  to  $-0.8$  Å were recorded with a dose rate of 8.6 e<sup>-</sup>/Å<sup>2</sup>/s. Each micrograph was exposed for 8 s, resulting in an accumulated dose of 68.8 e<sup>-</sup>/Å<sup>2</sup> and a total of 40 frames per stack, using SerialEM.

#### 4.6. Cryo-EM image processing and 3D reconstruction

Movies were motion-corrected with dose weighting using MotionCor2 [24]. The remainder of the processing was performed in RELION 3.0. Contrast transfer function (CTF) was determined using CTFIND4.1 (512 box size, 30 Å minimum resolution, 5 Å maximum resolution, 0.10 amplitude contrast) [25].

For ACSL1 in lipid nanodiscs: RELION 3.0's Laplacian-of-Gaussian was used to automatically pick an initial set of particles that were then subjected to reference-free 2D classification [26]. The best classes that represented views of ACSL1 in lipid nanodiscs were then used for template-based particle picking. A total of 176,167 particles were extracted (1.156 Å/pixel, 150-pixel box size) from 798 dose-weighted micrographs and subjected to reference-free 2D classification using a 256 Å mask diameter. The best 2D class averages showing a range of views were selected and subjected to more rounds of reference-free 2D classification. 2D classification results showed classes with ACSL1 broken off from the nanodisc as well as classes with ACSL1 in complex with the nanodisc. Since classes with ACSL1 alone (no nanodisc) showed higher resolution, we used a truncated version of ACSL1 that did not require the nanodisc to examine the ACSL1 structure to greater resolution.

For  $\Delta 58$  ACSL1: Aligned micrographs with a CTF max resolution above 8.0 were eliminated from further processing. Manual picking was used to pick an initial subset (about 7500 particles) that were then extracted (224-pixel box size) and subjected to reference-free 2D classification. The best seven classes that represented various views of ACSL1 were then used for template-based particle picking. From 2708 dose-weighted micrographs, 682,548 particles were extracted and binned 4  $\times$  4 (2.516 Å/pixel, 56-pixel box size) and subjected to reference-free 2D classification using a 120 Å mask diameter. The best 2D class averages showing top/bottom and side views were selected and subjected to more rounds of reference-free 2D classification using a 110 Å mask diameter. The best 2D class averages showing secondary-structure and multiple views were selected (83,000 particles) for further processing and were recentered and reextracted unbinned (0.629 Å/pixel, 224-pixel box size). An *ab initio* map generated in RELION without symmetry imposed (C1) was low-pass-filtered to 60 Å and was used as an initial reference map for 3D classification with C1 symmetry and four classes. 3D classification revealed that most particles separated into one of two classes, representing a possible closed (52%) and an open (26%) conformation (as judged by the differing positions of the C-terminal domain relative to the N-terminal domain). The stable classes showing the potential closed conformation (44,125 particles) and open conformation (21,620 particles) showed detailed secondary structure and were each subjected to 3D refinement. Postprocessing (sharpening and masking) resulted in a closed conformation map that was low-pass-filtered to a resolution of 10 Å and adjusted to a threshold of 0.0013 and an open conformation map that was low-pass-filtered to a resolution of 10 Å and adjusted to a threshold of 0.0027 using UCSF Chimera [27]. The previously solved *Mycobacterium tuberculosis* fatty acyl-CoA synthetase crystal structure (PDB ID: 3R44) [8] was visualized and measured in Chimera in order to compare the size and shape of the monomer to our 3D reconstruction. Figures were prepared using UCSF Chimera.

#### Author contributions

**Ning Wu:** conceptualization, data curation, formal analysis, funding acquisition, investigation, methodology, project administration, resources, supervision, validation, visualization, writing – original draft preparation, writing – review and editing. **Holly Dykstra:** data curation, formal analysis, investigation, methodology, software, visualization, writing – original draft preparation, writing – review and editing. **Chelsea Fisk:** formal analysis, investigation. **Cassi LaRose:** investigation, methodology. **Althea Waldhart:** investigation. **Xing Meng:** formal analysis, methodology, software, writing – review and editing. **Gongpu Zhao:** methodology, resources, software.

#### Declaration of competing interest

The authors declare that they have no competing interests.

#### Acknowledgments

This work was supported by Van Andel Institute funding to NW. We also thank Ruda de Luna Almeida Santos (Van Andel Institute) for technical assistance with cryo-EM sample preparation and image processing and David Nadziejka (Van Andel Institute) for critical reading of the manuscript.

#### Appendix A. Supplementary data

Supplementary data to this article can be found online at <https://doi.org/10.1016/j.abb.2021.108773>.

#### References

- [1] M. Lopes-Marques, I. Cunha, M.A. Reis-Henriques, M.M. Santos, L.F. Castro, Diversity and history of the long-chain acyl-CoA synthetase (Acsl) gene family in vertebrates, *BMC Evol. Biol.* 13 (2013) 271.
- [2] D.G. Mashek, L.O. Li, R.A. Coleman, Rat long-chain acyl-CoA synthetase mRNA, protein, and activity vary in tissue distribution and in response to diet, *J. Lipid Res.* 47 (2006) 2004–2010.
- [3] P.A. Young, C.E. Senkal, A.L. Suchanek, T.J. Grevengoed, D.D. Lin, L. Zhao, A. E. Crunk, E.L. Klett, J. Fullekrug, L.M. Obeid, et al., Long-chain acyl-CoA synthetase 1 interacts with key proteins that activate and direct fatty acids into niche hepatic pathways, *J. Biol. Chem.* 293 (2018) 16724–16740.
- [4] F. Gao, X.F. Yang, N. Fu, Y. Hu, Y. Ouyang, K. Qing, Roles of long-chain acyl coenzyme A synthetase in absorption and transport of fatty acid, *Chin. Med. Sci. J.* 31 (2016) 62–64.
- [5] J.M. Ellis, L.O. Li, P.C. Wu, T.R. Koves, O. Ilkayeva, R.D. Stevens, S.M. Watkins, D. M. Muoio, R.A. Coleman, Adipose acyl-CoA synthetase-1 directs fatty acids toward beta-oxidation and is required for cold thermogenesis, *Cell Metabol.* 12 (2010) 53–64.
- [6] K. Lee, J. Kerner, C.L. Hoppel, Mitochondrial carnitine palmitoyltransferase 1a (CPT1a) is part of an outer membrane fatty acid transfer complex, *J. Biol. Chem.* 286 (2011) 25655–25662.
- [7] Y. Hisanaga, H. Ago, N. Nakagawa, K. Hamada, K. Ida, M. Yamamoto, T. Hori, Y. Arai, M. Sugahara, S. Kuramitsu, et al., Structural basis of the substrate-specific two-step catalysis of long chain fatty acyl-CoA synthetase dimer, *J. Biol. Chem.* 279 (2004) 31717–31726.
- [8] C.S. Andersson, C.A. Lundgren, A. Magnusdottir, C. Ge, A. Wieslander, D. Martinez Molina, M. Hogbom, The *Mycobacterium tuberculosis* very-long-chain fatty acyl-CoA synthetase: structural basis for housing lipid substrates longer than the enzyme, *Structure* 20 (2012) 1062–1070.
- [9] G. Kochan, E.S. Pilka, F. von Delft, U. Oppermann, W.W. Yue, Structural snapshots for the conformation-dependent catalysis by human medium-chain acyl-coenzyme A synthetase ACSM2A, *J. Mol. Biol.* 388 (2009) 997–1008.
- [10] I.G. Denisov, S.G. Sligar, Nanodiscs for structural and functional studies of membrane proteins, *Nat. Struct. Mol. Biol.* 23 (2016) 481–486.
- [11] J.M. Dorr, S. Scheidelaar, M.C. Koorengel, J.J. Dominguez, M. Schafer, C.A. van Walree, J.A. Killian, The styrene-maleic acid copolymer: a versatile tool in membrane research, *Eur. Biophys. J.* 45 (2016) 3–21.
- [12] J. Frauenfeld, R. Loving, J.P. Armache, A.F. Sonnen, F. Guettou, P. Moberg, L. Zhu, C. Jegerschold, A. Flayhan, J.A. Briggs, et al., A saposin-lipoprotein nanoparticle system for membrane proteins, *Nat. Methods* 13 (2016) 345–351.
- [13] S.A. Abdelmagid, S.E. Clarke, D.E. Nielsen, A. Badawi, A. El-Sohemy, D.M. Mutch, D.W. Ma, Comprehensive profiling of plasma fatty acid concentrations in young healthy Canadian adults, *PLoS One* 10 (2015), e0116195.

- [14] E.L. Klett, S. Chen, A. Yechool, F.B. Lih, R.A. Coleman, Long-chain acyl-CoA synthetase isoforms differ in preferences for eicosanoid species and long-chain fatty acids, *J. Lipid Res.* 58 (2017) 884–894.
- [15] E. D'Imprima, D. Floris, M. Joppe, R. Sanchez, M. Grininger, W. Kuhlbrandt, Protein denaturation at the air-water interface and how to prevent it, *Elife* 8 (2019).
- [16] R.M. Glaeser, Proteins, interfaces, and cryo-em grids, *Curr. Opin. Colloid Interface Sci.* 34 (2018) 1–8.
- [17] L. Moody, G.B. Xu, H. Chen, Y.X. Pan, Epigenetic regulation of carnitine palmitoyltransferase 1 (Cpt1a) by high fat diet, *Biochim Biophys Acta Gene Regul Mech* 1862 (2019) 141–152.
- [18] D.W. Foster, Malonyl-CoA: the regulator of fatty acid synthesis and oxidation, *J. Clin. Invest.* 122 (2012) 1958–1959.
- [19] A. Faye, C. Esnous, N.T. Price, M.A. Onfray, J. Girard, C. Prip-Buus, Rat liver carnitine palmitoyltransferase 1 forms an oligomeric complex within the outer mitochondrial membrane, *J. Biol. Chem.* 282 (2007) 26908–26916.
- [20] Z.A. Jenei, K. Borthwick, V.A. Zammit, A.M. Dixon, Self-association of transmembrane domain 2 (TM2), but not TM1, in carnitine palmitoyltransferase 1A: role of GXXXG(A) motifs, *J. Biol. Chem.* 284 (2009) 6988–6997.
- [21] Z.A. Jenei, G.Z. Warren, M. Hasan, V.A. Zammit, A.M. Dixon, Packing of transmembrane domain 2 of carnitine palmitoyltransferase-1A affects oligomerization and malonyl-CoA sensitivity of the mitochondrial outer membrane protein, *Faseb. J.* 25 (2011) 4522–4530.
- [22] S.H. Scheres, RELION: implementation of a Bayesian approach to cryo-EM structure determination, *J. Struct. Biol.* 180 (2012) 519–530.
- [23] D.N. Mastronarde, Automated electron microscope tomography using robust prediction of specimen movements, *J. Struct. Biol.* 152 (2005) 36–51.
- [24] S.Q. Zheng, E. Palovcak, J.P. Armache, K.A. Verba, Y. Cheng, D.A. Agard, MotionCor2: anisotropic correction of beam-induced motion for improved cryo-electron microscopy, *Nat. Methods* 14 (2017) 331–332.
- [25] A. Rohou, N. Grigorieff, CTFFIND4: fast and accurate defocus estimation from electron micrographs, *J. Struct. Biol.* 192 (2015) 216–221.
- [26] J. Zivanov, T. Nakane, B.O. Forsberg, D. Kimanius, W.J. Hagen, E. Lindahl, S. H. Scheres, New tools for automated high-resolution cryo-EM structure determination in RELION-3, *Elife* 7 (2018).
- [27] E.F. Pettersen, T.D. Goddard, C.C. Huang, G.S. Couch, D.M. Greenblatt, E.C. Meng, T.E. Ferrin, UCSF Chimera—a visualization system for exploratory research and analysis, *J. Comput. Chem.* 25 (2004) 1605–1612.